NMR Superdense Coding with Quantum State Tomography

Edwin Ng*
MIT Department of Physics
(Dated: May 18, 2012)

We demonstrate the experimental implementation of two-qubit superdense coding on liquid-state NMR spectroscopy of chloroform. To verify the success of the protocol, we employ the technique of quantum state tomography to reconstruct the density matrix of the state for the preparation, encoding, and decoding stages. We quantify the quality of the implementation using the fidelity measure of quantum states, and we observe the decrease in fidelity upon introducing a delay between encoding and decoding. The analysis technique we use for tomography and a description of error estimations are discussed in detail.

I. INTRODUCTION AND THEORY

The implementation of simple quantum logic gates and algorithms using techniques in nuclear magnetic resonance (NMR) spectroscopy is explored in Junior Lab Experiment 49,[1] an account of which is summarized in [2]. In the same spirit, we develop here the ubiquitous technique of quantum state tomography for NMR quantum information processing and then utilize this technique to demonstrate the implementation of the quantum superdense coding protocol.

A very similar experiment has been performed in 2000 by Fang, et al., and our experimental procedures and interpretations will be in loose parallel to their work in [3]. Any notation not defined in this paper will follow the conventions used in [2].

I.1. Superdense Coding

We first introduce the *Bell states* for two qubits:

$$|\Phi^+\rangle = \frac{|00\rangle + |11\rangle}{\sqrt{2}} \quad |\Psi^+\rangle = \frac{|01\rangle + |10\rangle}{\sqrt{2}}$$
$$|\Phi^-\rangle = \frac{|00\rangle - |11\rangle}{\sqrt{2}} \quad |\Psi^-\rangle = \frac{|01\rangle - |10\rangle}{\sqrt{2}}.$$

Suppose now that Alice holds the first qubit and Bob holds the second qubit, and that Alice and Bob prepare their qubits in the initial state $|\Phi^+\rangle$.

Superdense coding is a quantum protocol which allows Alice to send to Bob two bits of classical information by performing operations only on her own qubit.[4] In fact, Alice needs only apply one of four operations to send the classical bitstrings 00, 01, 10, and 11:

$$\begin{aligned} 00:\ I_1|\Phi^+\rangle = |\Phi^+\rangle \quad & 01:\ X_1^2|\Phi^+\rangle = |\Psi^+\rangle \\ 10:\ Z_1^2|\Phi^+\rangle = |\Phi^-\rangle \quad & 11:\ Y_1^2|\Phi^+\rangle = |\Psi^-\rangle, \end{aligned} \tag{1}$$

up to irrelevant overall phases and where the subscript 1 denotes that nothing is done to qubit 2. We see that Alice can change the mutual quantum state into any of the four Bell states; this is the *encoding stage*. Since the Bell states form a complete orthonormal basis, Alice can then send her qubit to Bob, and Bob can simply measure the total system in the Bell basis to determine the operation Alice applied; this is the *decoding stage*.

To prepare the mutual state, we use the sequence[4]

$$U = Y_2 U_\tau \overline{X}_2 X_1, \tag{2}$$

which maps the initial state $|00\rangle$ into $|\Psi^+\rangle$, up to an overall phase. After the preparation, we apply the encoding sequence precisely as defined in Equation 1, except we take $Z_1^2 = X_1^2 Y_1^2$, up to an overall phase.

To measure the encoded state, we actually perform the inverse of the preparation sequence, and then measure in the computational basis. We use the inverse

$$U^\dagger = \overline{X}_1 X_2 U_\tau^3 \overline{Y}_2. \tag{3}$$

It can be shown that $U^\dagger$ maps the Bell states to

$$U^\dagger|\Phi^+\rangle = |00\rangle \quad U^\dagger|\Psi^+\rangle = |01\rangle$$
$$U^\dagger|\Phi^-\rangle = |10\rangle \quad U^\dagger|\Psi^-\rangle = |11\rangle,$$

up to irrelevant overall phases. The bitstring labels of the computational basis then precisely gives the encoded classical bitstrings, completing the decoding process.

I.2. Quantum State Tomography

Measurement in NMR is made primarily through the FID readout. Suppose that the state after the computation is described by the density matrix ρ. The most general measurement we can do is to first apply a *readout operator* R and then measure the FID of one spin.[4]

The FID due to spin k after application of readout R is mathematically described by[1]

$$V_k(R;t) = -\operatorname{tr}\left[e^{-iHt} R\,\rho\, R^\dagger e^{iHt}\left(i\sigma_x^{(k)} + \sigma_y^{(k)}\right)\right]. \tag{4}$$

The superscripts on the Pauli operators mean they act only on spin k. In this lab, $k = 1$ denotes qubit 1 (hydrogen) and $k = 2$ qubit 2 (carbon).

* ngedwin@mit.edu

When working with the pseudo-pure state $\overline{\rho}$ created via temporal averaging, then we sum the FIDs of the temporal averaging process and use the linearity of trace.[5] Since we will deal only with pseudo-pure states in superdense coding, we use ρ to denote the simulated $\overline{\rho}$.

If ρ is expected to be diagonal (i.e., a mixed state involving only the pseudo-pure computational basis states), then it suffices to obtain the FID readouts $V_1(X_1;t)$ and $V_2(X_2;t)$ and solve a system of equations to reconstruct the diagonals of ρ, as was done in [2].

Generalizing these readout operators allows the full reconstruction of the density matrix, a technique called *quantum state tomography*.[4] To perform state tomography, we utilize the following FID readouts, which according to [6] is a sufficient set.

We recall that Equation 4 gives two oscillators at frequencies $\omega_k \pm J/2$, with amplitudes proportional to differences among the matrix elements ρ_{ij}. As in Experiment 49, we are interested in the Fourier-transformed FIDs, which gives two spectral lines with integrals equal to the (complex) amplitudes. Using Equation 5, we get a system of equations for reconstructing ρ.

$$
\begin{aligned}
V_1(X_1;t) &= [(\rho_{11}-\rho_{33})+i(-\rho_{31}-\rho_{13})]\, e^{i(\omega_1-J/2)t} + [(\rho_{22}-\rho_{44})+i(-\rho_{42}-\rho_{24})]\, e^{i(\omega_1+J/2)t} \\
V_1(X_2;t) &= [(\rho_{14}-\rho_{23})+i(-\rho_{13}-\rho_{24})]\, e^{i(\omega_1-J/2)t} + [(\rho_{23}-\rho_{14})+i(-\rho_{24}-\rho_{13})]\, e^{i(\omega_1+J/2)t} \\
V_2(X_1;t) &= [(\rho_{14}-\rho_{32})+i(-\rho_{12}-\rho_{34})]\, e^{i(\omega_2-J/2)t} + [(\rho_{32}-\rho_{14})+i(-\rho_{12}-\rho_{34})]\, e^{i(\omega_2+J/2)t} \\
V_2(X_2;t) &= [(\rho_{11}-\rho_{22})+i(-\rho_{21}-\rho_{12})]\, e^{i(\omega_2-J/2)t} + [(\rho_{33}-\rho_{44})+i(-\rho_{43}-\rho_{34})]\, e^{i(\omega_2+J/2)t} \\
V_1(Y_1;t) &= i(\rho_{31}-\rho_{13}-\rho_{11}+\rho_{33})e^{i(\omega_1-J/2)t} + i(+\rho_{42}-\rho_{24}-\rho_{22}+\rho_{44})e^{i(\omega_1+J/2)t} \\
V_1(Y_2;t) &= i(\rho_{13}-\rho_{14}+\rho_{23}-\rho_{24})e^{i(\omega_1-J/2)t} + i(-\rho_{14}-\rho_{13}-\rho_{23}-\rho_{24})e^{i(\omega_1+J/2)t} \\
V_2(Y_1;t) &= i(\rho_{14}-\rho_{12}-\rho_{34}+\rho_{32})e^{i(\omega_2-J/2)t} + i(-\rho_{12}-\rho_{14}-\rho_{32}-\rho_{34})e^{i(\omega_2+J/2)t} \\
V_2(Y_2;t) &= i(\rho_{21}-\rho_{12}-\rho_{11}+\rho_{22})e^{i(\omega_2-J/2)t} + i(+\rho_{43}-\rho_{34}-\rho_{33}+\rho_{44})e^{i(\omega_2+J/2)t}
\end{aligned}
\tag{5}
$$

II. EXPERIMENTAL SETUP AND PROCEDURE

The experiment runs on a Bruker Advance 200 NMR spectrometer with a sample of 7% by weight $^{13}CHCl_3$ dissolved in d6-acetone and controlled through a MATLAB interface, as described in [1] and summarized in [2].

The calibration procedure for this experiment involves the calculation of phase references ϕ_1 and ϕ_2, 90° pulse widths for H and C, and normalization factors N_c and N to account for the effects of the amplifier circuits. We use the same procedure for these calibrations as in [2] (except that the step size used for pulse width calibration is 0.1 µs instead of 0.25 µs).

For this experiment, we find $\phi_1 = 231.44° \pm 0.15°$ and $\phi_2 = 234.46° \pm 0.24°$. The 90° pulse widths are found to be (9.30 ± 0.08)µs for H and (8.31 ± 0.08)µs for C. The normalization factors are $N_c = 3.16 \pm 0.05$ and $N = (6.38 \pm 0.03) \times 10^{-9}$. For consistency, we use the hardcoded value of $J = 214.9613$ Hz used by the MATLAB interface in temporal averaging.

To verify the superdense coding protocol, we perform four sets of tomography experiments:

1. One on the pseudo-pure initial state $|00\rangle$;
2. One on the prepared state $|\Phi^+\rangle$;
3. One for each encoded Bell state, for classical messages 0, 1, 2, and 3; and
4. One for each decoded computational basis state, for classical messages 0, 1, 2, and 3.

This yields a total of ten tomograms, which consists of eight FIDs each (4 readouts × 2 nuclei), following Equation 5. Each FID takes approximately three minutes to acquire (3 sequences for one temporal averaged FID × 50 s delay per pulse sequence). Thus, total runtime is approximately four hours.

Finally, we also perform an experiment exploring the effects of a delay Δt on the order of the decoherence time $T_2^* \approx 0.2$ s [2] between encoding and decoding. Because of time restrictions, we decide to perform this only on the superdense coding of the message 00, which should be representative of the others.

The procedure is a standard tomograph, but repeated with varying values of Δt. We use the values between 0 s to 0.5 s, in steps of 0.02 s, yielding 26 tomograms with a runtime of ten hours, covered in two runs: one going up to 0.2 s and the second (two days later but with the same calibration parameters) from there up to 0.5 s.

III. ANALYSIS OF ERRORS

We introduce several modifications to the error estimates of the peak integrals beyond the simple statistical uncertainties used in [2], to account for the systematic uncertainties going into the fit procedure of Section IV.

First, because we now generally expect zero peaks, which are not sharply localized in frequency, we increase the integration range to 25 Hz, using trapezoidal integration as before. We sample the standard deviation of the FID outside the peak regions and use that value as uniform uncertainties on all points in the FID, which are propagated into the integral.

To account for the signal-to-noise ratio and for any possible zero offset in the FID, we also compute the (complex) RMS of the signal outside the peaks, treating the left and right peaks separately. This is then multiplied by twice the integration range and added as systematic uncertainty into the peak integral uncertainties.

Because of the ambiguity of which integration range to use, we also compute the peak integrals using the previous 5 Hz range used in [2] and in calibrations, along with the standard 50 Hz range used by the MATLAB interface. We take half the difference between the two results as an additional source of systematic uncertainty.

Next, we consider possible systematic effects due to pulsing. Although the statistical uncertainty on the parabolic fit $y = ax^2 + bx + c$ is generally small, there is a discrepancy between the pulse widths x_l and x_r given by the left and right peaks respectively. In quoting pulse widths, we provide the average of $x = (x_l + x_r)/2$ and include the discrepancy as the systematic part of δx.

However, the effect of this uncertainty on the peak integrals has been largely ignored in [2]. As a first approximation, we estimate the signal error δy due to this discrepancy as $\delta y = (a_l + a_r)(\delta x)^2$. This formula comes about by taking the second-order Taylor expansion $2a(\delta x)^2$ of the fits about their respective maxima to determine the change in y as a result of δx. We then average the effects from both the left and right peaks to arrive at our formula for δy.

For this experiment, we find $\delta y = 5.7 \times 10^3$ for H and $\delta y = 380$ for C. The units are arbitrary because we have not yet normalized the peak integrals; however this is on the order of 1% of a maximal peak integral, which is approximately 10^6 and 10^5 for H and C, respectively.

Since this is a systematic error from pulsing, we also want to take into account the number of pulses applied. Using some rough estimation, we count 15 rotation gates used in temporal averaging. In the preparation sequence U, we use one for H and two for C (and the same for $U^\dagger$). For encoding, we use two gates for encoding 01 and 11 and four gates (from $Z_1^2 = X_1^2 Y_1^2$) for encoding 10 (none are used for 00).

We then compute the total systematic uncertainty due to pulsing as the number of gates squared times δy. Again, the square comes from the fact that as the pulse errors accumulate, the signal loss is roughly quadratic.

Finally, we multiply both the peak integrals and their total uncertainties by the normalization factors N and N_c, as done in [2]. We also propagate the statistical uncertainties in N and N_c by quadrature, separately for real and imaginary parts.

IV. DENSITY MATRIX RECONSTRUCTION

The process described in Section III gives us 16 complex peak integrals (8 FIDs with left and right peak integrals) with statistical and systematic uncertainties accounted for, which we can use for reconstructing ρ.

One way to solve the tomography problem is to simply perform a least-squares linear solution. We find, however, that such a solution does not generally satisfy the constraints that density matrices be positive-semidefinite (Hermitian with nonnegative eigenvalues) operators with trace one. Thus, a general complex matrix is not a suitable model for our data.

Rather, following a suggestion in [7], we introduce the matrix T, defined to be

$$T = \begin{bmatrix} x_1 & x_2 + ix_{11} & x_3 + ix_{12} & x_4 + ix_{13} \\ 0 & x_5 & x_6 + ix_{14} & x_7 + ix_{15} \\ 0 & 0 & x_8 & x_9 + ix_{16} \\ 0 & 0 & 0 & x_{10} \end{bmatrix}$$

where the x_k are real parameters. If we now define $\rho = T^\dagger T$, we are guaranteed that ρ is positive-semidefinite. Furthermore, since the diagonals of ρ are real, we can save imposing the trace condition until the very end. The trade-off, of course, is that our fit needs to be nonlinear, as the elements of ρ which go into Equation 5 are no longer linear functions of the parameters x_j.

In order to avoid fitting complex numbers, we separate the 16 complex amplitudes from Section III into real and imaginary components, giving us a data set Y_j of 32 points, which we fit to the 16 parameters x_k. The fitting function takes in the x_k, generates T, computes ρ, and applies Equation 5 with real and imaginary parts separated to obtain the fit function $\overline{Y}_j$.

All of this is done numerically, and we use an algorithm for nonlinear chi-square fitting with uncertainties written by Brahms,[8] which runs on native MATLAB procedures and provides uncertainty estimates δx_j on the parameters. From the uncertainties δx_j, we easily obtain the uncertainties δT on T. We then define the uncertainty on ρ to be $\delta\rho = (\delta T)^\dagger T + T^\dagger(\delta T)$, taking the absolute value of the real and imaginary parts.

Finally, although we can judge the quality of the result by simply plotting the density matrix as a 3D bar graph and checking for qualitative agreement with the predicted result, we pursue a more quantitative measure using the the *fidelity* of the state. As defined by [4], the fidelity of a density matrix with respect to an expected pure state ψ is given by

$$F(|\psi\rangle) = \sqrt{\langle\psi|\rho|\psi\rangle}. \tag{6}$$

To estimate the uncertainty on the fidelity, we take

$$\delta F = \frac{\sqrt{|\langle\psi|\,\mathrm{Re}[\delta\rho]^2|\psi\rangle|}}{2F}. \tag{7}$$

Detailed properties of the fidelity as a measure of quantum state distances are given in [4], but we note here that the closer the fidelity is to one, the closer ρ is to $|\psi\rangle$.

V. RESULTS AND DISCUSSION

We show an explicit fit for the prepared state $|\Psi^+\rangle$ to all 32 Y_j in Figure 1 below, to illustrate the nature of the fitting function and to demonstrate the error bars resulting from the error estimates of Section III.

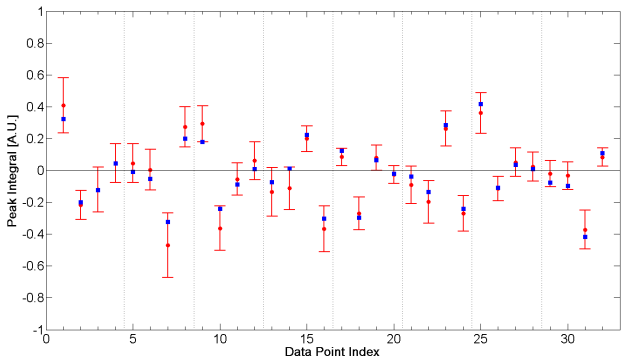

FIG. 1. A fit of the 32 peak integrals for the tomography of $|\Phi^+\rangle$, where the red circles represent the measured data set Y_j and the blue squares represent the fitted points $\overline{Y}_j$. Note the partitioning into groups of four: the partitions represent the readouts X_1, Y_1, X_2, and Y_2 for H followed by the same for C. Within each partition, we order the four points by real left and right peaks and then imaginary left and right peaks.

For the initial pure state $|00\rangle$, we find that we obtain a fidelity of 0.89 ± 0.06 with a $\chi^2_{16} = 0.55$, while for the prepared state $|\Phi^+\rangle$, we have a fidelity of 0.83 ± 0.07 and a $\chi^2_{16} = 0.48$. We do not have room to accomodate the density matrix plots for these two preparation tomographs, but we note that they are similar to their corresponding states in the encoding and decoding of 00 in Figures 2 and 3.

Although these states are not used to demonstrate superdense coding, they do give very useful benchmarks for the fidelity measure. From the tomography of $|00\rangle$, which involves no pulse sequences, we see that temporal averaging and the readout operator already accounts for a large drop in fidelity from the ideal case. From the tomography of $|\Phi^+\rangle$, we also see that U has an effect on fidelity as well, and that the creation of pseudo-Bell states incurs a cost in quality, possibly due to the U_τ gate used.

We show the real parts of the reconstructed ρ for each of the classical messages of the encoding protocol in Figure 2, where we expect to see density matrices corresponding to the four Bell states. Below that, in Figure 3, we show the real parts of the reconstructed ρ for each of the classical messages after decoding. We expect to obtain the computational basis states. We do not show the imaginary parts of ρ because they are generally less than 0.1 and do not show any interesting or notable structure.

For clarity, we also do not show the error bars on the density matrices. However, they are generally between 5% to 40%, with most elements settling at around 15% of the total density matrix element. It is clear that due to our generous estimation of errors in Section III, our tomographed density matrices are not very precise. Nevertheless, at least on the qualitative level, we can see that they clearly demonstrate the correctness, if not robustness, of superdense coding.

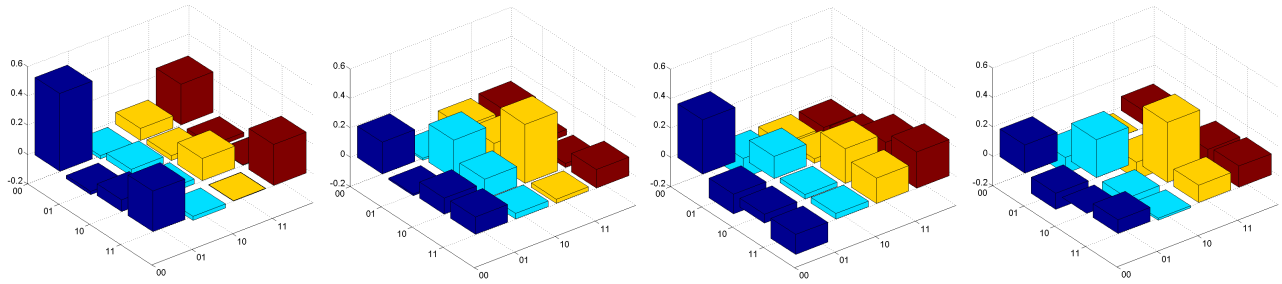

(a)Encoding 00 (b)Encoding 01 (c)Encoding 10 (d)Encoding 11

FIG. 2. Real part of the reconstructed density matrix for the superdense encoding protocol.

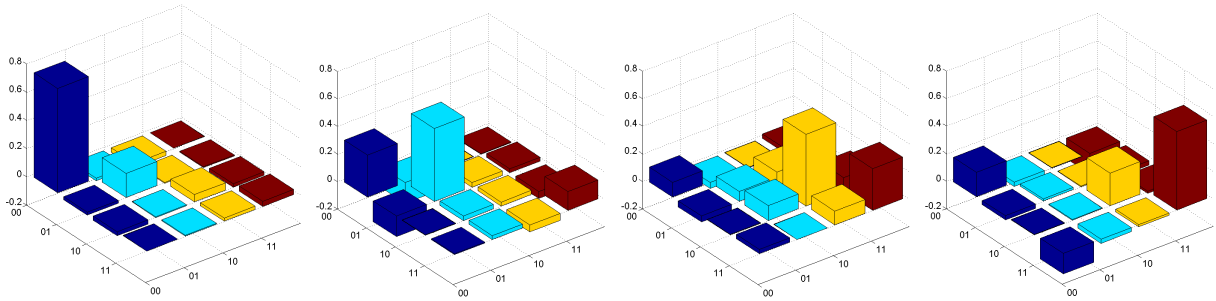

(a)Decoding 00 (b)Decoding 01 (c)Decoding 10 (d)Decoding 11

FIG. 3. Real part of the reconstructed density matrix for the superdense decoding protocol.

In fact, we can do a little better by employing the measure of fidelity. In Tables I and II, we show fidelity measures between different states, according to Equations 6 and 7. We see that, at least between the possible alternatives, the one we expect to get wins out in terms of fidelity. This, of course, points to an objective method for Bob to decode Alice's message: he computes the fidelity of the decoded state against each of the computational basis states and takes the one with the highest fidelity.

Code	χ^2_{16}	$F(\|\Phi^+\rangle)$	$F(\|\Psi^+\rangle)$	$F(\|\Phi^-\rangle)$	$F(\|\Psi^-\rangle)$
00	.49	$\mathbf{.82 \pm .07}$	$.36 \pm .12$	$.25 \pm .07$	$.36 \pm .06$
01	.86	$.54 \pm .16$	$\mathbf{.68 \pm .14}$	$.45 \pm .08$	$.22 \pm .08$
10	1.51	$.51 \pm .22$	$.47 \pm .13$	$\mathbf{.67 \pm .08}$	$.27 \pm .21$
11	1.70	$.41 \pm .16$	$.47 \pm .09$	$.40 \pm .05$	$\mathbf{.66 \pm .05}$

TABLE I. Chi-squared of fits and fidelity measures across different possible Bell states for the encoded density matrices. The dominant fidelity is bolded for reference.

Code	χ^2_{16}	$F(\|00\rangle)$	$F(\|01\rangle)$	$F(\|10\rangle)$	$F(\|11\rangle)$
00	.66	$\mathbf{.86 \pm .06}$	$.41 \pm .08$	$.23 \pm .03$	$.20 \pm .07$
01	.71	$.55 \pm .08$	$\mathbf{.73 \pm .10}$	$.17 \pm .09$	$.37 \pm .09$
10	1.23	$.33 \pm .07$	$.27 \pm .12$	$\mathbf{.72 \pm .23}$	$.55 \pm .02$
11	.75	$.42 \pm .07$	$.13 \pm .09$	$.49 \pm .17$	$\mathbf{.75 \pm .06}$

TABLE II. Chi-squared of fits and fidelity measures across different possible basis states for the decoded density matrices. The dominant fidelity is bolded for reference.

It is interesting to note that at the decoding stage, the poorest fit and the one with (arguably) the lowest fidelity is the $|10\rangle$ state, which is subjected to the most pulses, due to the Z_1^2 used in the encoding stage. This suggests that a 180° pulse is not the same as two 90° pulses, which could cause the encoding of 10 to be more noisy.

Another interesting fact is that the fidelity goes *up* upon decoding. This could mean that applying the inverse circuit $U^\dagger$ actually undoes some of the accumulated errors. In fact, between encoding and decoding of the message 00, $|00\rangle$ went down by only 0.03 in fidelity.

This leads to our final experiment: the introduction of a delay time between encoding and decoding, to see if we can get this fidelity to go down as we add a delay Δt between setting up $|\Phi^+\rangle$ and decoding to recover $|00\rangle$.

A plot of the fidelity of the decoded state against $|00\rangle$ as a function of Δt is shown in Figure 4. Note that the point at 60 ms is suspect because the fit does not converge well on that point; nevertheless, it occupies an unremarkable point on the trend and seems to fit in well, so we retain it for completeness.

The general trend is, as expected, a decreasing function of Δt, with an apparent asymptotic value above 0.5. However, it is more interesting to note the possibility that there is additional structure in the plot, with noticeable upward fluctuations around 40 ms, 80 ms, 340 ms, and 460 ms. Their origins are unknown.

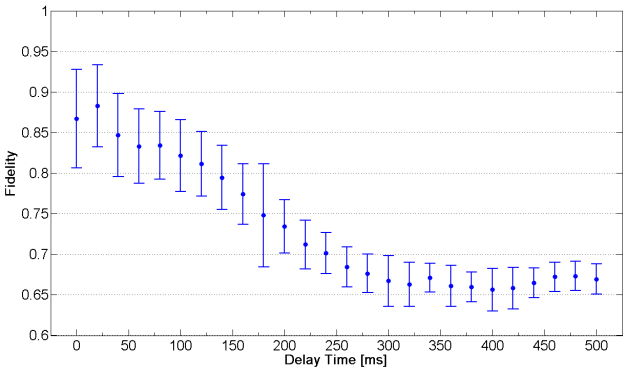

FIG. 4. Fidelity of the decoded $|00\rangle$ state as a function of the delay time Δt between encoding and decoding. Note the apparent structure in the trend.

VI. CONCLUSIONS

In meeting the terms of our proposal, we succeeded in developing a technique for performing quantum state tomography on NMR of two qubits and demonstrated its use in implementing the superdense coding protocol. We also introduced the use of fidelity as a means of quantifying the quality of tomographed states and showed that it is a valid measure by verifying its decay as we subject the system to decoherence.

[1] M.I.T. Junior Lab Staff, "Quantum Information Processing with NMR," (2011).
[2] E. Ng, "NMR Quantum Information Processing," (2012).
[3] X. Fang, X. Zhu, M. Feng, X. Mao, and F. Du, "Experimental implementation of dense coding using nuclear magnetic resonance," Phys. Rev. A **61** (2000).
[4] I.L. Chuang and M.A. Nielsen, *Quantum Computation and Quantum Information* (University Press, 2000).
[5] I.S. Oliveira, T.J. Bonagamba, et al., *NMR Quantum Information Processing* (Elsevier, 2007).
[6] J.S. Lee, "The quantum state tomography on an NMR system," Phys. Lett. A **305**, 349–353 (2002).
[7] A. Niggebaum, *Quantum State Tomography of the 6 qubit photonic symmetric Dicke State*, Master's thesis, University of Munich (2011).
[8] N. Brahms, "*MATLAB File Exchange*: Generalized Nonlinear Chi-Square Fitting," (2009), (Algorithm).

ACKNOWLEDGMENTS

EN gratefully acknowledges his lab partner, Polnop Samutpraphoot, and the Junior Lab staff for their assistance in understanding the theory behind the design and analysis of this experiment.